JOURNAL OF PHYSICAL OCEANOGRAPHY

Exploring the role of the "Ice-Ocean governor" and mesoscale eddies in the equilibration of the Beaufort Gyre: lessons from observations

GIANLUCA MENEGHELLO *, EDWARD DODDRIDGE, JOHN MARSHALL, JEFFERY SCOTT, JEAN-MICHEL CAMPIN

Department of Earth, Atmospheric and Planetary Sciences, Massachusetts Institute of Technology, Cambridge, Massachusetts 02139-4307, USA.

ABSTRACT

Observations of Ekman pumping, sea surface height anomaly, and isohaline depth anomaly over the Beaufort Gyre are used to explore the relative importance and role of (i) feedbacks between ice and ocean currents, dubbed the "Ice-Ocean governor" and (ii) mesoscale eddy processes in the equilibration of the Beaufort Gyre. A two-layer model of the gyre is fit to observations and used to explore the mechanisms governing the gyre evolution from the monthly to the decennial time scale. The Ice-Ocean governor dominates the response on inter-annual timescales, with eddy processes becoming evident only on the longest, decadal timescales.

1. Introduction

The Arctic Ocean's Beaufort Gyre, centered in the Canada Basin, is a large-scale, wind-driven, anticyclonic circulation pattern characterized by a strong halocline stratification with relatively fresh surface waters overlying saltier (and warmer) waters of Atlantic Ocean origin. The halocline stratification inhibits the vertical flux of ocean heat to the overlying sea ice cover. Ekman pumping associated with a persistent but highly variable Arctic high pressure system (Proshutinsky and Johnson 1997; Proshutinsky et al. 2009, 2015; Giles et al. 2012) accumulates freshwater and inflates isopycnals. The induced isopycnal slope drives a geostrophically balanced flow whose imprint can be clearly seen in the doming of sea surface height at the center of the Beaufort Sea (see Figure 1).

Recent observational studies by Meneghello et al. (2017, 2018b); Dewey et al. (2018); Zhong et al. (2018), have outlined how the interaction between the ice and the surface current plays a central role in the equilibration of the Beaufort Gyre's geostrophic current intensity and its freshwater content. Downwelling-favorable winds and ice motion inflate the gyre until the relative velocity between the geostrophic current and the ice velocity is close to zero, at which point the surface-stress-driven Ekman pumping is turned off, and the gyre inflation is halted. In Meneghello et al. (2018a) we developed a theory describing this negative feedback between the ice drift and the ocean currents. We called it the "ice-ocean governor" by analogy with mechanical governors that regulate the speed of engines and other devices through dynamical feedbacks (Maxwell 1867; Bennet 1993; Murray et al. 2018).

Another mechanism at work, studied by Davis et al. (2014); Manucharyan et al. (2016, 2017); Meneghello et al. (2017), and mimicking the mechanism of equilibration hypothesized for the ACC by Marshall et al. (2002); Karsten et al. (2002), relies on eddy fluxes to release freshwater accumulated by the persistent anticyclonic winds blowing over the gyre. In this scenario, representing the case of ice in free-drift, or the case of an ice free gyre, the Ice-Ocean governor does not operate and the gyre inflates until baroclinic instability is strong enough to balance the freshwater input.

In this study, we start from observations and address how both mechanisms interact in a real-world Arctic, where we expect their role to change over the seasonal cycle as ice cover and ice mobility vary. A theory for their combined role in the equilibration of the Beaufort Gyre has been recently proposed by Doddridge et al. (2019). We begin by assimilating time series of Ekman pumping, inferred from observations (see Meneghello et al. 2018b), and sea surface height, obtained from satellite measurements (Armitage et al. 2016, see Figure 1a) into a two-layer model of the Beaufort Gyre (see Figure 2). Despite its limitations, as we shall see our model is able to capture much of the observed variability of the gyre. We then evaluate the relative role of the Ice-Ocean governor and eddy

Corresponding author address: Department of Earth, Atmospheric and Planetary Sciences, Massachusetts Institute of Technology, Cambridge, Massachusetts 02139-4307, USA.
E-mail: gianluca.meneghello@gmail.com

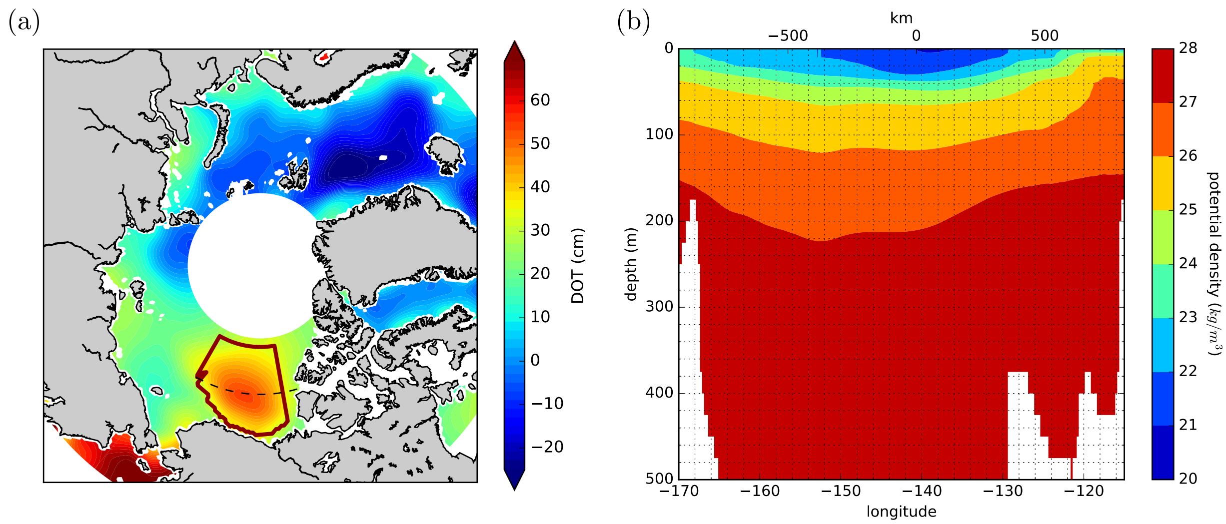

FIG. 1. a) The doming of satellite-derived Dynamic Ocean Topography (DOT) marks the persistent anticyclonic circulation the Beaufort Gyre, one of the main features of the Arctic Ocean (color, 2003-2014 mean, data from Armitage et al. (2016)). The white area is beyond the 81.5°N latitudinal limit of the Envisat satellite. The Beaufort Gyre Region used for computations in this study, including only locations within 70.5° − 80.5°N and 170° − 130°W whose depth is greater than 300 m, is marked by the thick red line. b) A section across the Beaufort Gyre Region at 75°N, marked by a dashed line in (a), shows how the doming up of the sea surface height toward the middle of the gyre is reflected in the potential density structure of the gyre which bows down in to the interior. The stratification is dominated by salinity variations and concentrated close to the surface, with potential densities ranging from a mean value of 1021 kg m^{-3} at the surface to close to 1028 kg m^{-3} at a depth of about 200 m, and remaining almost constant below that.

fluxes in equilibrating the gyre's isopycnal depth anomaly, and its freshwater content. We conclude by using these new insights to discuss how changes in the Arctic ice cover will impact the state of the Beaufort gyre.

2. Two-layer model of the Beaufort Gyre

Let us consider a two-layer model comprising the sea surface height η and isopycnal depth anomaly a, as shown in Figure 2 (for a description of the model, see Section 12.4 of Cushman-Roisin and Beckers 2010). For time scales T longer than one day ($Ro_T = \frac{1}{fT} < 0.1$, where $f = 1.45 \times 10^{-4}\,\mathrm{s}^{-1}$ is the Coriolis parameter, and is assumed constant) and length scales L larger than 5 km ($Ro = \frac{U}{fL} < 0.1$, where $U \approx 5\,\mathrm{cm\,s}^{-1}$ is a characteristic velocity), currents in the interior of the Beaufort Gyre can be considered in geostrophic balance everywhere except at the very top and bottom of the water column, where frictional effects drive a divergent Ekman transport. The dynamics of the sea surface height and isopycnal depth anomalies can then be approximated by

$$\begin{aligned} \frac{d(\eta - a)}{dt} &= -K\frac{a}{R^2} - \underbrace{\overline{w}_{Ek}}_{\text{Top Ekman}} \\ \frac{da}{dt} &= K\frac{a}{R^2} + \underbrace{\frac{d}{2f}\frac{g\eta + g'a}{R^2}}_{\text{Bottom Ekman}}, \end{aligned} \tag{1}$$

where $\frac{1}{R^2}$ represent a scaling for the laplacian operator. Volume is gathered and released by the surface Ekman pumping $\overline{w}_{Ek} = \frac{1}{A}\int_A \frac{\nabla\times\tau}{\rho f}dA$, proportional to the curl of the surface stress $\boldsymbol{\tau}$, and by the bottom Ekman pumping $-\frac{d}{2f}\frac{g\eta+g'a}{R^2}$, proportional to the Ekman layer length scale d and driven by the bottom geostrophic current $\frac{\hat{k}}{f}\times\nabla(g\eta+g'a)$ (see Section 8.4 of Cushman-Roisin and Beckers 2010).

The term $K\frac{a}{R^2}$ represents mesoscale eddies and vertical diffusivity acting to flatten density surfaces, such that $K = K_h + \frac{R^2}{\delta^2}K_v$, where K_h is the isopycnal thickness diffusivity, R is a representative horizontal length scale, K_v is the diapycnal diffusivity, and δ is a representative vertical length scale for the halocline. Multiplying K_v by $\frac{R^2}{\delta^2}$ converts the vertical diffusivity into an equivalent horizontal diffusivity.

The reference water density is taken as $\rho = 1028\,\mathrm{kg\,m}^{-3}$, and g and $g' = \frac{\Delta\rho}{\rho}g$ are the gravity and reduced gravity constants, with $\Delta\rho$ the difference in between the potential density at the surface and at depth.

For the purpose of our discussion we consider the surface stress $\boldsymbol{\tau}$, to have a wind-driven $\boldsymbol{\tau}_a$ and an ice-driven $\boldsymbol{\tau}_i$ component, weighted by the ice concentration α

$$\boldsymbol{\tau} = (1-\alpha)\underbrace{\rho_a C_{Da}|\boldsymbol{u}_a|\boldsymbol{u}_a}_{\boldsymbol{\tau}_a} + \alpha\underbrace{\rho C_{Di}|\boldsymbol{u}_i - \boldsymbol{u}_g|(\boldsymbol{u}_i - \boldsymbol{u}_g)}_{\boldsymbol{\tau}_i}, \tag{2}$$

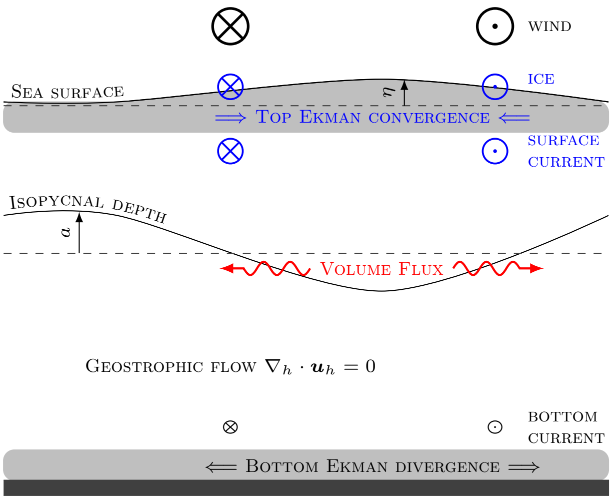

FIG. 2. Schematic of the idealized two-layer model: the wind- and ice-driven Ekman flow (blue) drives variations in the layer thicknesses or, equivalently, in the sea surface height η and isopycnal depth a. The interior is assumed to be in geostrophic balance, and eddy and mixing processes (red) result in a volume flux between the two layers flattening the isopycnal slope.

where $\boldsymbol{u}_a$, $\boldsymbol{u}_i$ and $\boldsymbol{u}_g$ are the wind, ice and surface geostrophic current velocities respectively, $\rho_a = 1.25\,\mathrm{kg\,m^{-3}}$ is the air density, and $C_{Da} = 0.00125$ and $C_{Di} = 0.0055$ are the air-ocean and ice-ocean drag coefficients. We note how the geostrophic surface currents $\boldsymbol{u}_g$ act as a negative feedback on the ice-driven component (see Meneghello et al. 2018a).

To better understand the relative role of the winds, sea-ice, ocean geostrophic currents, and eddy diffusivity in the equilibration of the gyre, we additionally compute the contribution of the geostrophic current to the ice stress as

$$\boldsymbol{\tau}_{ig} = \boldsymbol{\tau}_i - \boldsymbol{\tau}_{i0}, \tag{3}$$

where $\boldsymbol{\tau}_{i0}$ is the ice-ocean stress neglecting the geostrophic current, i.e., computed by setting $\boldsymbol{u}_g = 0$ in (2). Accordingly, we define the Ekman pumping associated with each component as

$$\begin{aligned} w_a &= \frac{\nabla\times((1-\alpha)\boldsymbol{\tau}_a)}{\rho f} & w_i &= \frac{\nabla\times(\alpha\boldsymbol{\tau}_i)}{\rho f} \\ w_{i0} &= \frac{\nabla\times(\alpha\boldsymbol{\tau}_{i0})}{\rho f} & w_{ig} &= \frac{\nabla\times(\alpha\boldsymbol{\tau}_{ig})}{\rho f}, \end{aligned} \tag{4}$$

so that the total Ekman pumping can be written as

$$w_{Ek} = w_a + w_i = w_a + w_{i0} + w_{ig}. \tag{5}$$

We also note that the eddy flux term $K\frac{a}{R^2}$, having units of $\mathrm{m\,year^{-1}}$, can be expressed as an equivalent Ekman pumping and compared with the other Ekman velocities.

The dynamics in (1) then describe a "wind-driven" Beaufort Gyre where water masses exhcanges are limited to Ekman processes at the top and bottom of the domain, with eddies and mixing redistributing volume internally.

An observationally-based estimate of the relative importance of the Ice-Ocean governor contribution w_{ig} and the eddy fluxes contribution $K\frac{a}{R^2}$ to the equilibration of the Beaufort Gyre is the main focus of our study.

3. Fitting parameters of the two-layer model using observations of the Beaufort Gyre

In order to estimate the key parameters, we drive the model (1) using observed Ekman pumping $\overline{w}_{Ek}$, averaged over the Beaufort Gyre Region (see Figure 1) and shown as a black curve in Figure 3a. We set $R = 300\,\mathrm{km}$, a characteristic length scale for the wind and ice velocity gradients — see, e.g., Figure 1 of Meneghello et al. (2018b). We then vary K, g', and d, as well as the initial conditions of sea surface height and isopycnal depth anomalies, to minimize the departure of the estimated sea surface height anomaly from the observed one, shown as a black curve in Figure 3b. The datasets used are described in Appendix A1. The procedure to estimate the 5 free parameters using the 144 monthly observational data points is outlined in Appendix A2. The estimated parameters, and their standard deviations, are $K = (218\pm31)\,\mathrm{m^2\,s^{-1}}$ and $g' = (0.065\pm0.007)\,\mathrm{m\,s^{-2}}$ (or, equivalently, $\Delta\rho = 6.8\,\mathrm{kg\,m^{-3}}$) broadly in accord with observations (see Meneghello et al. 2017, and Figure 1b). The estimated bottom Ekman layer thickness $d = (58\pm11)\,\mathrm{m}$ includes bathymetry effects which cannot be represented in our model.

The estimated sea surface height anomaly (Figure 3b, blue) closely follows the observed one (black) (RMSE $= 0.02\,\mathrm{m}$, $R^2 = 0.68$) and captures relatively well both the seasonal cycle and the relatively sudden changes in sea surface height and isopycnal depth anomaly that occurred in 2007 and 2012, both associated with changes in the ice extent and atmospheric circulation (McPhee et al. 2009; Simmonds and Rudeva 2012). As should be expected, the isopycnal depth anomaly (red) responds to the forcing at longer time scales, and has a smaller variability, than the sea surface height. Red squares mark the observed August September October mean 30 psu isohaline depth anomaly, corresponding to the surface layer depth anomaly (see Proshutinsky et al. 2018), and are not used in the data estimation process.

Our simple model estimates a single constant value of eddy diffusivity for the entire Beaufort Gyre region. Previous work on the Beaufort Gyre has suggested that the eddy diffusivity vary in space (Meneghello et al. 2017) and depends on the state of the large-scale flow (Manucharyan et al. 2016), while studies focussing on the Southern Ocean have shown that eddy diffusivity varies in both space and time (Meredith and Hogg 2006; Wang and Stewart 2018). Similarly, in our computation of Ekman

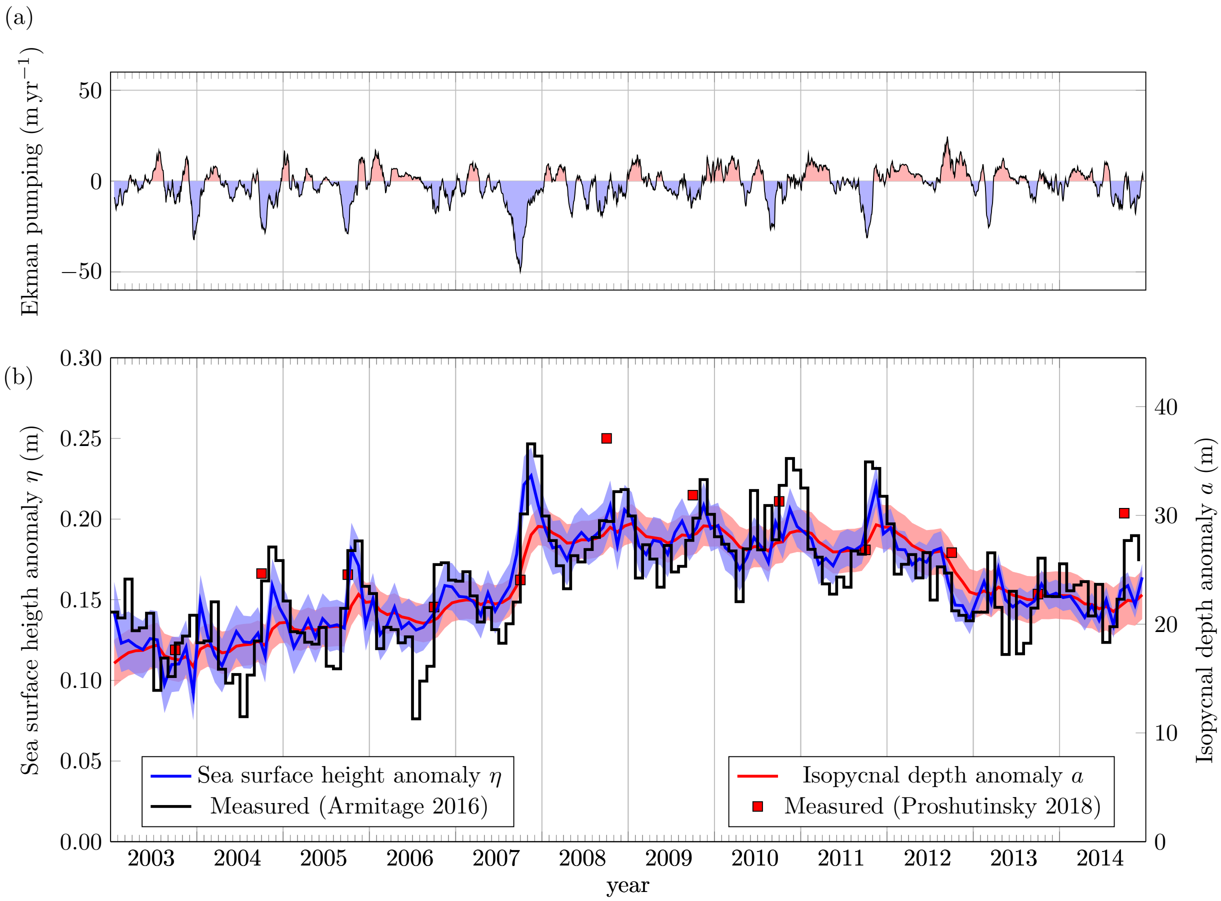

FIG. 3. Observations of monthly mean Ekman pumping (black, top panel) and mean sea surface height anomaly (black, bottom panel) over the Beaufort Gyre Region are assimilated in the idealized model (1). Blue and red filled areas in the top panel denotes upwelling and downwelling respectively. Red marks shows the 30 psu isohaline depth anomaly estimated from hydrographic data for August-September-October of each year (Proshutinsky et al. 2009, 2018); in the Arctic, isohaline depth can be considered a good approximation to isopycnal depth because the ocean stratification is mostly due to salinity variations. The estimated sea surface height anomaly (blue), isopycnal depth anomaly (red), eddy diffusivity $K = 218\,\mathrm{m^2\,s^{-1}}$ and reduced gravity $g' = 0.065\,\mathrm{m\,s^{-2}}$ (corresponding to $\Delta\rho = 6.8\,\mathrm{kg\,m^{-3}}$) are in agreement with observations. In particular, the estimated sea surface height anomaly (blue) captures most of the observed seasonal cycle variability (black) as well as its long-term increase after 2007 (RMSE $=$ 0.02 m, $R^2 = 0.68$). The estimated bottom Ekman layer thickness is $d = 58\,\mathrm{m}$, and includes the effects of bottom bathymetry. Shaded blue and red regions in the bottom panel show the uncertainty of the model estimation (one standard deviation).

pumping (Meneghello et al. 2018b) we assume a constant value for the drag coefficient despite the fact that observational evidence suggest a large variability (Cole et al. 2017). Despite its limitations, our model is able to capture much of the observed variability of the gyre over the time period considered, and will be used in the next section to discuss the relative role of the governor and eddy fluxes in the gyre equilibration.

4. Relative importance of the Ice-Ocean governor and eddy fluxes

Now that parameters of our model (1) have been estimated using available observations, we can analyze the different role of each term in the equilibration of the Beaufort Gyre. Figure 4a shows monthly running means of wind-driven w_a and ice-driven w_{i0} downwelling favorable Ekman pumping (cumulative mean of $-12.2\,\mathrm{m\,year^{-1}}$, dark and light blue respectively). This is to be compared with the deflating effect of eddy fluxes $K\frac{a}{R^2}$ (equivalent to a mean upwelling of $1.8\,\mathrm{m\,year^{-1}}$, dark red) and of the upwelling favorable Ice-Ocean governor Ekman pumping w_{ig} (mean of $9.8\,\mathrm{m\,year^{-1}}$ upwards, light red). Over the 12 years of the available data, the contribution of the governor, reducing freshwater accumulation by limiting Ekman downwelling, is six times larger than the freshwater release associated with eddy fluxes. The small residual Ekman pumping of $-0.6\,\mathrm{m\,year^{-1}}$ accounts for the 7 m increase in isopycnal depth between 2003 and 2014 (red line

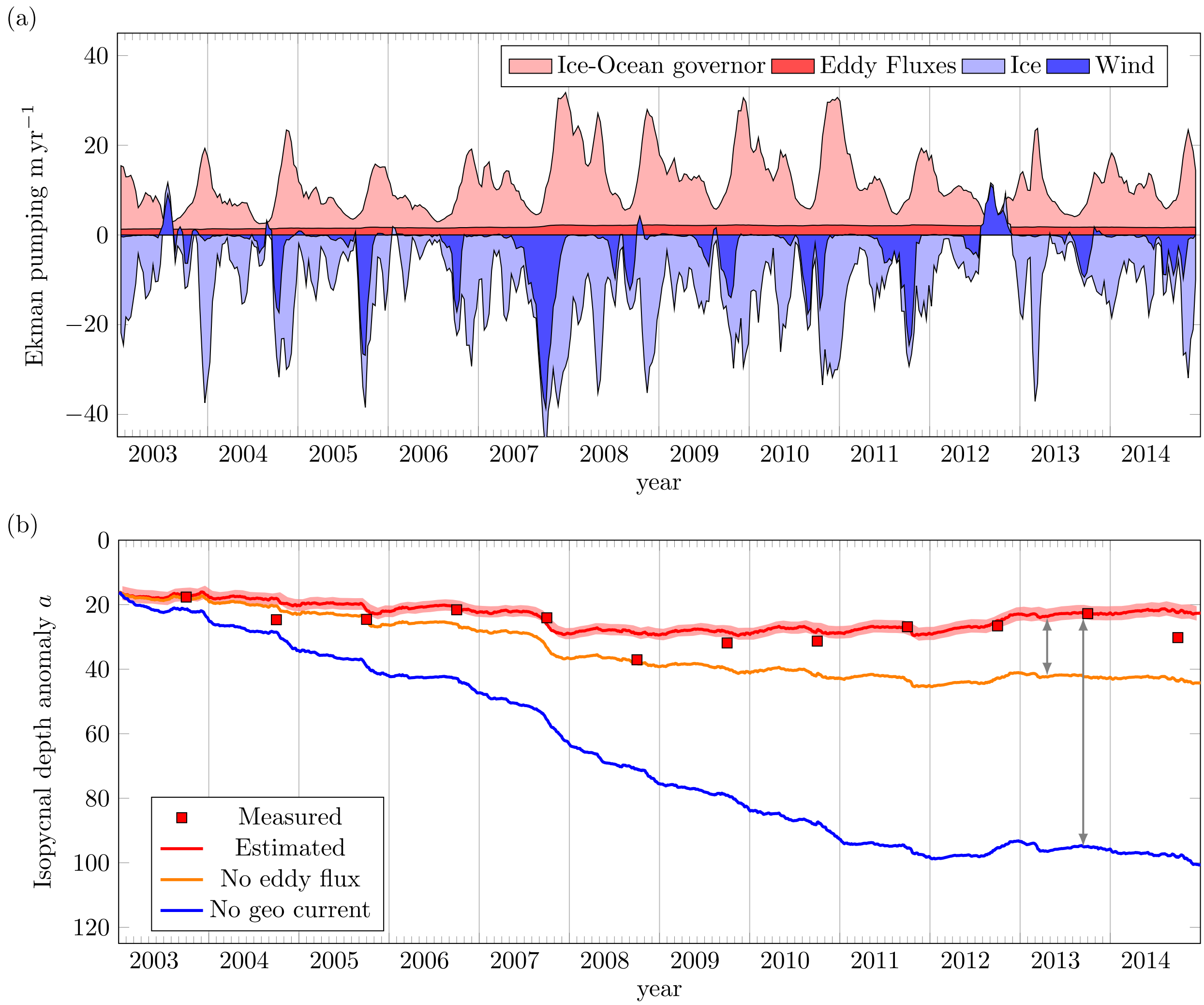

FIG. 4. a) Ekman pumping associated with wind forcing w_a (dark blue) ice forcing w_{i0} (light blue), eddy fluxes $K\frac{a}{R^2}$ (dark red) and the Ice-Ocean governor w_{ig} (light red). See equation (4). The mean Ice-Ocean governor term w_{ig} is six times larger than the mean eddy fluxes term Ka/R^2. b) hypothetical isopycnal depth anomaly under different hypotheses: red line and red marks are the same as in Figure 3b, with the red shaded region denoting one standard deviation. The orange curve represents the evolution of the isopycnal obtained by neglecting eddy diffusivity in equation (1). The blue curve is obtained by neglecting the ice-ocean governor. The error introduced by not including the ice-ocean governor is much larger (gray arrows), with an increase in isopycnal depth anomaly more than ten times larger the actual one over the 12-year period considered.

in Figure 3b), consistent with observations (Proshutinsky et al. 2018).

The Ice-Ocean governor, acting on both barotropic (fast) and baroclinic (slower) timescales, plays a much larger role than that of eddy fluxes. As can be seen from Figure 4, the upwelling effect of the Ice-Ocean governor (light red) closely mirrors the downwelling effect of the ice motion (light blue), both having important variations over the seasonal cycle, and essentially canceling the net Ekman pumping over the ice covered regions of the gyre. In contrast, eddy fluxes provide a much smaller, but persistent, mechanism releasing the accumulated freshwater and flattening isopycnals.

To gain further insights into the different role played by the two mechanisms in the equilibration of the gyre, Figure 4b shows the hypothetical evolution of the isopycnal depth anomaly when neglecting eddy fluxes (orange) and when neglecting the Ice-Ocean governor (i.e., setting $w_{Ek} = w_a + w_{i0}$), but keeping the eddy diffusivity unchanged at $K = 218\,\mathrm{m^2\,s^{-1}}$ (blue). In both cases, we integrate the gyre model (1) using daily values of Ekman pumping (Meneghello et al. 2018b), starting from the same sea surface height and isopycnal depth anomaly on January 1st, 2003. It is clear how the isopycnal depth anomaly change between 2003 and 2014, estimated in the absence of the ice-ocean governor and with realistic values of eddy diffusivity, would have been more than 10 times the actual value of 7 m, while the error introduced by neglecting the eddy diffusivity would be much smaller.

5. Conclusions

Using observational estimates of Ekman pumping (Meneghello et al. 2017) and sea surface height anomaly (Armitage et al. 2016) we have estimated key parameters of a two layer model, and studied the relative effect of eddy fluxes and of the Ice-Ocean governor on the equilibration of the Beaufort Gyre. Both mechanisms have been previously addressed separately in both theoretical and observational settings by Davis et al. (2014); Manucharyan et al. (2016, 2017); Meneghello et al. (2017) and by Meneghello et al. (2018a,b); Dewey et al. (2018); Zhong et al. (2018); Kwok et al. (2013). Here, however, we have brought the two together in the context of observations, and used those observations to explore the relative importance of the two mechanisms.

In the current state of the Arctic, the Ice-Ocean governor plays a much more significant role than eddy fluxes in regulating the gyre intensity and its freshwater content. As can be inferred from Figure 4, this is particularly true on seasonal-to-interannual timescales. We judge that the freshwater not accumulated (by reduced Ekman downwelling) or released (by Ekman upwelling) by the Ice-Ocean governor is more than five times the freshwater released by eddies. This reminds us of how central is the interaction of ice with the underlying ocean in setting the timescale of response of the gyre and its ability to store fresh water. Moreover, this is a very difficult process to capture in models because it demands that we faithfully represent internal lateral stresses within the ice.

Future circulation regimes will be impacted by the changes in the concentration, thickness and mobility of ice that have significantly evolved over the past two decades. In particular, loss of multi-year ice and increased seasonality of the Arctic sea ice extent is to be expected, with summers characterized by ice-free or very mobile ice conditions, and winters characterized by an extensive ice cover (Haine and Martin 2017). Depending on the internal strength of winter-ice, the Arctic Ocean could evolve in the following two rather different scenarios. If the ice is very mobile then the present seasonal cycle of upwelling and downwelling (red and blue shaded areas in Figure 3) would be replaced by persistent, year-long downwelling. This would result in an increase in the depth of the halocline and more accumulation of fresh water. Ultimately the gyre would be stabilized through expulsion of fresh water from the Beaufort Gyre via enhanced eddy activity. However, if winter ice remains rigid, downwelling in the summer will be balanced by upwelling in the winter as the anticyclonic gyre rubs up against the winter-ice cover; stronger geostrophic currents will potentially result in stronger upwelling cycles, affecting the ocean stratification and increasing the variability of the isopycnal depth, geostrophic current and freshwater content over the seasonal cycle. Our ability to predict these changes depends on how well our models can represent the transfer of stress from the wind to the underlaying ocean, through the seasonal cycle of ice formation and melting.

Acknowledgments. The authors thankfully acknowledge support from NSF Polar Programs, both Arctic and Antarctic, and the MIT-GISS collaborative agreement.

APPENDIX

A1. Data

In order to constrain the model (1), we use observational estimates of Ekman pumping $\overline{w}_{Ek}$ and sea surface height anomaly η, summarized in Table A1.

Ekman pumping is shown in Figure 3a, where blue and red shading denote downwelling and upwelling time periods respectively. We remark how the presence of winter upwelling is a direct consequence of the inclusion of the geostrophic current in our estimates, is in agreement with results from Dewey et al. (2018) and Zhong et al. (2018), and lower than previous estimates by Yang (2006, 2009). The monthly time series of Ekman pumping used in this work is obtained by averaging our Arctic-wide observational estimates (Meneghello et al. 2017, 2018b) over the Beaufort Gyre Region (BGR, see Figure 1), and are thus based on sea ice concentration α from Nimbus-7 SMMR and DMSP SSM/I–SSMIS passive microwave data, version 1 (Cavalieri et al. 1996), sea ice velocity $\boldsymbol{u}_i$ from the Polar Pathfinder daily 25-km Equal-Area Scalable Earth Grid (EASE-Grid) sea ice motion vectors, version 3 (Tschudi et al. 2016), geostrophic currents $\boldsymbol{u}_g$ computed from dynamic ocean topography (Armitage et al. 2016, 2017), and 10-m wind $\boldsymbol{u}_a$ from the NCEP–NCAR Reanalysis 1 (Kalnay et al. 1996).

The mean sea surface height anomaly, shown by a black line in Figure 3b, is computed as the norm of the gradient of sea surface height estimates by Armitage et al. (2016), multiplied by $R = 300\,\text{km}$, a characteristic length scale for the wind and ice velocity gradients —– see, e.g., Figure 1 of Meneghello et al. (2018b). The original sea surface height estimate is available on a $0.75^\circ \times 0.25^\circ$ grid, and is obtained by combining Envisat (2003–2011) and CryoSat-2 (2012–2014) observations of sea surface height from the open ocean and ice-covered ocean (via leads). A total of 1761 grid points from the original dataset are used to compute the BGR-averaged sea surface height anomaly for each month.

While not used to constrain the model, an estimate of the mean isohaline depth anomaly, shown as red marks in Figure 3b, is obtained in a similar fashion. We start from the 50 km resolution August-September-October 30 psu isohaline depth estimated by Proshutinsky et al. (2018) using CTD, XCTD, and UCTD profiles collected each year from July through October, and available at `http://www.whoi.edu/page.do?pid=161756`. The norm of the isohaline gradient is averaged over the BGR and multiplied by the reference length $R = 300\,\mathrm{km}$. A total of 409 grid points are used to compute the BGR-averaged isohaline depth anomaly for each month.

A2. Parameter estimation

In this section we report the Matlab code and the data (Table A1) used for the parameter estimation.

```
% load Ekman pumping (we) and
% sea surface height (DOT)
% from table A1
infile = readtable('table1.dat');
we     = infile.wemonthly;
eta    = infile.eta;

% time step is 1 month
dt     = 3600*24*365/12.;

% initialize Matlab data object
z      = iddata(DOT,we,dt)

% initialize estimation options
greyopt        = greyestOptions;
greyopt.Focus  = 'simulation';

% initialize Linear ODE model
% with identifiable parameters
% - K    : eddy diffusivity
% - d    : bottom Ekman layer depth
% - drho : potential density anomaly
pars    = {'K',300;'d',100;'drho',6};
sysinit = idgrey('model',pars,'c');

% estimate parameters
[sys,x0]    = greyest(z,sysinit,greyopt);

% the linear ODE model (see equation 1)
function [A,B,C,D] = model(K,d,drho,Ts)
rho    = 1028.;        % reference density
f      = 1.45e-4;      % coriolis parameter
g      = 9.81;         % gravity constant
gp     = g*drho/rho;   % reduced gravity
R      = 300000.;      % reference radius
c1     = d/(2*f)/R^2;

A = [ -c1*g ,  c1*gp         ;
+c1*g , -c1*gp - K/R^2  ];
B = [-1 ; 0];
C = [ 1 , 0];
D = [ 0 ];
end
```

TABLE A1. Monthly sea surface height anomaly η (in m) and Ekman pumping (in $\mathrm{m\,year^{-1}}$) used in the parameter estimation.

year	mo.	η	$\overline{w}_{Ek}$	year	mo.	η	$\overline{w}_{Ek}$
2003	1	0.142	-7.398	2009	1	0.202	4.703
2003	2	0.139	-6.615	2009	2	0.163	5.557
2003	3	0.163	-3.450	2009	3	0.184	-1.023
2003	4	0.131	-1.674	2009	4	0.175	-0.829
2003	5	0.133	-5.032	2009	5	0.158	2.681
2003	6	0.142	-3.644	2009	6	0.184	-5.403
2003	7	0.094	10.883	2009	7	0.167	-8.091
2003	8	0.114	1.349	2009	8	0.171	-1.080
2003	9	0.102	0.444	2009	9	0.187	-4.655
2003	10	0.123	-5.263	2009	10	0.201	-10.915
2003	11	0.127	10.102	2009	11	0.224	-1.338
2003	12	0.140	-21.177	2009	12	0.203	-2.539
2004	1	0.123	-5.422	2010	1	0.189	4.489
2004	2	0.124	1.785	2010	2	0.184	4.651
2004	3	0.149	4.182	2010	3	0.180	7.557
2004	4	0.107	-2.673	2010	4	0.149	1.247
2004	5	0.098	-7.644	2010	5	0.182	-5.933
2004	6	0.104	-2.659	2010	6	0.218	-2.027
2004	7	0.077	-2.116	2010	7	0.181	2.846
2004	8	0.103	-4.836	2010	8	0.208	-11.050
2004	9	0.124	3.382	2010	9	0.187	-3.376
2004	10	0.162	-20.013	2010	10	0.221	-12.391
2004	11	0.183	-8.052	2010	11	0.238	-4.079
2004	12	0.174	-2.140	2010	12	0.230	-1.687
2005	1	0.149	6.352	2011	1	0.219	0.154
2005	2	0.130	-0.034	2011	2	0.181	7.473
2005	3	0.130	-4.991	2011	3	0.176	3.002
2005	4	0.124	1.538	2011	4	0.160	3.893
2005	5	0.122	-5.125	2011	5	0.153	-2.333
2005	6	0.133	-1.683	2011	6	0.164	-3.340
2005	7	0.109	-2.172	2011	7	0.158	-2.162
2005	8	0.107	-0.960	2011	8	0.180	-3.641
2005	9	0.145	-25.463	2011	9	0.178	-12.486
2005	10	0.180	-14.042	2011	10	0.235	-19.021
2005	11	0.186	7.576	2011	11	0.231	0.646
2005	12	0.158	-2.855	2011	12	0.214	-1.992
2006	1	0.154	8.651	2012	1	0.197	4.682
2006	2	0.120	2.786	2012	2	0.166	2.914
2006	3	0.133	-4.002	2012	3	0.172	6.189
2006	4	0.131	3.300	2012	4	0.178	2.075
2006	5	0.123	0.110	2012	5	0.164	1.992
2006	6	0.127	2.032	2012	6	0.179	-2.718
2006	7	0.076	0.169	2012	7	0.150	-3.338
2006	8	0.100	-3.141	2012	8	0.170	7.610
2006	9	0.109	-5.783	2012	9	0.167	12.183
2006	10	0.172	-11.716	2012	10	0.143	8.439
2006	11	0.173	-8.533	2012	11	0.140	9.761
2006	12	0.162	-3.639	2012	12	0.137	0.691
2007	1	0.161	-2.895	2013	1	0.142	-5.709
2007	2	0.167	-1.076	2013	2	0.142	1.986
2007	3	0.152	2.955	2013	3	0.179	-9.708
2007	4	0.136	-5.348	2013	4	0.145	2.228
2007	5	0.145	1.314	2013	5	0.116	3.331
2007	6	0.131	-3.571	2013	6	0.155	0.169
2007	7	0.123	-6.748	2013	7	0.116	1.155
2007	8	0.135	-15.367	2013	8	0.123	-1.203
2007	9	0.149	-33.312	2013	9	0.145	-6.684
2007	10	0.203	-27.466	2013	10	0.176	-1.592
2007	11	0.247	-11.235	2013	11	0.152	-2.489
2007	12	0.239	-1.104	2013	12	0.152	-0.927
2008	1	0.202	4.239	2013	1	0.172	-1.570
2008	2	0.187	1.943	2014	2	0.156	1.486
2008	3	0.171	5.061	2014	3	0.159	4.149
2008	4	0.157	-2.798	2014	4	0.161	-1.120
2008	5	0.177	-5.266	2014	5	0.140	3.293
2008	6	0.173	-1.955	2014	6	0.160	-4.453
2008	7	0.181	-3.670	2014	7	0.124	4.210
2008	8	0.189	-5.542	2014	8	0.133	-8.139
2008	9	0.199	-11.426	2014	9	0.150	-7.954
2008	10	0.199	3.454	2014	10	0.187	-0.192
2008	11	0.217	-9.181	2014	11	0.190	-9.237
2008	12	0.218	-4.953	2014	12	0.174	0.337

References

Armitage, T. W. K., S. Bacon, A. L. Ridout, A. A. Petty, S. Wolbach, and M. Tsamados, 2017: Arctic Ocean geostrophic circulation 2003-2014. *The Cryosphere Discussions*, **2017**, 1–32, doi:10.5194/tc-2017-22, URL http://www.the-cryosphere-discuss.net/tc-2017-22/.

Armitage, T. W. K., S. Bacon, A. L. Ridout, S. F. Thomas, Y. Aksenov, and D. J. Wingham, 2016: Arctic sea surface height variability and change from satellite radar altimetry and GRACE, 2003-2014. *Journal of Geophysical Research: Oceans*, **121 (6)**, 4303–4322, doi:10.1002/2015JC011579.

Bennet, S., 1993: *A history of control engineering, 1930-1955*. IET, 262 pp., doi:10.1049/PBCE047E.

Cavalieri, D. J., C. L. Parkinson, P. Gloersen, and H. J. Zwally, 1996: Sea Ice Concentrations from Nimbus-7 SMMR and DMSP SSM/I-SSMIS Passive Microwave Data, Version 1. NASA National Snow and Ice Data Center Distributed Active Archive Center, Boulder, Colorado USA, doi:10.5067/8GQ8LZQVL0VL.

Cole, S. T., and Coauthors, 2017: Ice and ocean velocity in the Arctic marginal ice zone: Ice roughness and momentum transfer. *Elementa: Science of the Anthropocene*, doi:10.1525/elementa.241.

Cushman-Roisin, B., and J.-M. Beckers, 2010: *Introduction to Geophysical Fluid Dynamics. Physical and Numerical Aspects*, Vol. 101. 786 pp., doi:10.1016/B978-0-12-088759-0.00022-5.

Davis, P., C. Lique, and H. L. Johnson, 2014: On the link between arctic sea ice decline and the freshwater content of the beaufort gyre: Insights from a simple process model. *Journal of Climate*, **27 (21)**, 8170–8184, doi:10.1175/JCLI-D-14-00090.1.

Dewey, S., J. Morison, R. Kwok, S. Dickinson, D. Morison, and R. Andersen, 2018: Arctic Ice-Ocean Coupling and Gyre Equilibration Observed With Remote Sensing. *Geophysical Research Letters*, doi:10.1002/2017GL076229, URL http://doi.wiley.com/10.1002/2017GL076229.

Doddridge, E. W., G. Meneghello, J. Marshall, and J. Scott, 2019: A Three-way Balance in The Beaufort Gyre: The Ice-Ocean Governor, Wind Stress, and Eddy Diffusivity. *Under review J. Geophys. Res. C: Oceans*.

Giles, K. A., S. W. Laxon, A. L. Ridout, D. J. Wingham, and S. Bacon, 2012: Western Arctic Ocean freshwater storage increased by wind-driven spin-up of the Beaufort Gyre. *Nature Geoscience*, **5 (3)**, 194–197, doi:10.1038/ngeo1379, URL http://www.nature.com/doifinder/10.1038/ngeo1379.

Haine, T. W., and T. Martin, 2017: The Arctic-Subarctic sea ice system is entering a seasonal regime: Implications for future Arctic amplification. *Scientific Reports*, **7 (1)**, 1–9, doi:10.1038/s41598-017-04573-0.

Kalnay, E., and Coauthors, 1996: The NCEP/NCAR 40-year reanalysis project. *Bulletin of the American Meteorological Society*, **77 (3)**, 437–471, doi:10.1175/1520-0477(1996)077⟨0437:TNYRP⟩2.0.CO;2, arXiv:1011.1669v3.

Karsten, R., H. Jones, and J. Marshall, 2002: The Role of Eddy Transfer in Setting the Stratification and Transport of a Circumpolar Current. *Journal of Physical Oceanography*, **32 (1)**, 39–54, doi:10.1175/1520-0485(2002)032⟨0039:TROETI⟩2.0.CO;2.

Kwok, R., G. Spreen, and S. Pang, 2013: Arctic sea ice circulation and drift speed: Decadal trends and ocean currents. *Journal of Geophysical Research: Oceans*, **118 (5)**, 2408–2425, doi:10.1002/jgrc.20191.

Manucharyan, G. E., M. A. Spall, and A. F. Thompson, 2016: A Theory of the Wind-Driven Beaufort Gyre Variability. *Journal of Physical Oceanography*, **(2013)**, 3263–3278, doi:10.1175/JPO-D-16-0091.1.

Manucharyan, G. E., A. F. Thompson, and M. A. Spall, 2017: Eddy Memory Mode of Multidecadal Variability in Residual-Mean Ocean Circulations with Application to the Beaufort Gyre. *Journal of Physical Oceanography*, **47 (4)**, 855–866, doi:10.1175/JPO-D-16-0194.1, URL http://journals.ametsoc.org/doi/10.1175/JPO-D-16-0194.1.

Marshall, J., H. Jones, R. Karsten, and R. Wardle, 2002: Can Eddies Set Ocean Stratification? *Journal of Physical Oceanography*, **32 (1)**, 26–38, doi:10.1175/1520-0485(2002)032⟨0026:CESOS⟩2.0.CO;2, URL http://dx.doi.org/10.1175/1520-0485(2002)032{\%}3C0026:CESOS{\%}3E2.0.CO{\%}5Cn2.

Maxwell, J. C., 1867: On Governors. *Proceedings of the Royal Society of London*, **16**, 270–283, doi:10.1098/rspl.1867.0055.

McPhee, M. G., A. Proshutinsky, J. H. Morison, M. Steele, and M. B. Alkire, 2009: Rapid change in freshwater content of the Arctic Ocean. *Geophysical Research Letters*, **36 (10)**, 1–6, doi:10.1029/2009GL037525.

Meneghello, G., J. Marshall, J.-M. Campin, E. Doddridge, and M.-L. Timmermans, 2018a: The Ice-Ocean governor: ice-ocean stress feedback limits Beaufort Gyre spin up. *Geophysical Research Letters*, **45**, 1–7, doi:10.1029/2018GL080171.

Meneghello, G., J. Marshall, S. T. Cole, and M.-L. Timmermans, 2017: Observational inferences of lateral eddy diffusivity in the halocline of the Beaufort Gyre. *Geophysical Research Letters*, **44**, 1–8, doi:10.1002/2017GL075126, URL http://doi.wiley.com/10.1002/2017GL075126.

Meneghello, G., J. Marshall, M.-L. Timmermans, and J. Scott, 2018b: Observations of seasonal upwelling and downwelling in the Beaufort Sea mediated by sea ice. *Journal of Physical Oceanography*, **48**, 795–805, doi:10.1175/JPO-D-17-0188.1.

Meredith, M. P., and A. M. Hogg, 2006: Circumpolar response of Southern Ocean eddy activity to a change in the Southern Annular Mode. *Geophysical Research Letters*, doi:10.1029/2006GL026499.

Murray, J., H. Bradley, W. Craigie, C. T. Onions, R. Burchfield, E. WEiner, and J. Simpson, 2018: governor. Oxford University Press.

Proshutinsky, A., D. Dukhovskoy, M.-l. Timmermans, R. Krishfield, and J. L. Bamber, 2015: Arctic circulation regimes. *Philosophical transactions. Series A, Mathematical, physical, and engineering sciences*, **373 (2052)**, 20140 160, doi:10.1098/rsta.2014.0160, URL http://rsta.royalsocietypublishing.org/content/373/2052/20140160.

Proshutinsky, A., and Coauthors, 2009: Beaufort Gyre freshwater reservoir : State and variability from observations. *Journal of Geophysical Research*, **114**, 1–25, doi:10.1029/2008JC005104.

Proshutinsky, A., and Coauthors, 2018: Summer freshwater content changes in the Beaufort Gyre Region from 2003 – 2017. *Under review*.

Proshutinsky, A. Y., and M. A. Johnson, 1997: Two circulation regimes of the wind-driven Arctic Ocean. *Journal of Geophysical Research: Oceans*, **102 (C6)**, 12 493–12 514, doi:10.1029/97JC00738.

Simmonds, I., and I. Rudeva, 2012: The great Arctic cyclone of August 2012. *Geophysical Research Letters*, **39 (23)**, 1–6, doi:10.1029/2012GL054259.

Tschudi, M., C. Fowler, J. S. Maslanik, and W. Meier, 2016: Polar Pathfinder Daily 25 km EASE-Grid Sea Ice Motion Vectors, Version 3. URL http://dx.doi.org/10.5067/O57VAIT2AYYY, doi:10.5067/O57VAIT2AYYY.

Wang, Y., and A. L. Stewart, 2018: Eddy dynamics over continental slopes under retrograde winds: Insights from a model intercomparison. *Ocean Modelling*, doi:10.1016/j.ocemod.2017.11.006, arXiv:1011.1669v3.

Yang, J., 2006: The seasonal variability of the Arctic Ocean Ekman transport and its role in the mixed layer heat and salt fluxes. *Journal of Climate*, **19 (20)**, 5366–5387, doi:10.1175/JCLI3892.1.

Yang, J., 2009: Seasonal and interannual variability of downwelling in the Beaufort Sea. *J Geophys Res*, **114**, C00A14, doi:10.1029/2008JC005084, URL http://dx.doi.org/10.1029/2008JC005084.

Zhong, W., M. Steele, J. Zhang, and J. Zhao, 2018: Greater Role of Geostrophic Currents in Ekman Dynamics in the Western Arctic Ocean as a Mechanism for Beaufort Gyre Stabilization. *Journal of Geophysical Research: Oceans*, doi:10.1002/2017JC013282, URL http://doi.wiley.com/10.1002/2017JC013282.